Influence of modelling and scenario uncertainties on the numerical simulation of a semi-industrial flameless furnace

Valentina Fortunato[1], Chiara Galletti[2*], Leonardo Tognotti[2], Alessandro Parente[1†]

1. *Service d'Aéro-Thermo-Mécanique, Université Libre de Bruxelles, Bruxelles, Belgium.*
2. *Dipartimento di Ingegneria Civile e Industriale, Università di Pisa, Pisa, ITALY*

Keywords: flameless combustion; MILD combustion; turbulence-chemistry interactions; uncertainty; validation

Revised manuscript
November 2014

[*] Corresponding Author: Dr. Chiara Galletti, Università di Pisa, Dipartimento di Ingegneria Civile e Industriale, Largo L. Lazzarino 2, I-56122 Pisa – Italy. Tel: +39 050 22 17 897. Fax: +39 050 22 17 866. Email: chiara.galletti@unipi.it.
[†] Corresponding Author: Dr. Alessandro Parente. Université Libre de Bruxelles, Service d'Aéro-Thermo-Mécanique, Avenue F. D. Roosevelt 50, B-1050 Bruxelles, Belgique Tel: +32 2 650 26 80. Fax: +32 2 650 27 10. Email : Alessandro.Parente@ulb.ac.be.

Abstract

Flameless combustion is able to provide high combustion efficiency with low NO_x and soot emissions. The present work aims at investigating the role of closure sub-models for the modelling of a flameless furnace, as well as the main NO formation paths. Among the different turbulence models that were tested, modified k-ε provides the best agreement with the experimental data, especially for temperature measurements. Reynolds stress model leads to smaller deviation for radial velocity predictions. Since in flameless combustion regime the turbulence-chemistry interaction as well as the kinetic mechanism play a fundamental role, the Eddy Dissipation Concept (EDC), coupled with four different kinetic schemes (JL, KEE58, GRI 2.11 and GRI 3.0) was considered. The GRI 2.11 and KEE58 mechanisms perform better, thus confirming the necessity of turbulence/chemistry interaction models accounting for finite-rate chemistry when flameless combustion is studied. As far as NO emissions are concerned, the N_2O intermediate NO mechanism is found to play a major role, while thermal NO formation mechanism is not as relevant as in traditional combustion regime.

An assessment of the uncertainty related to the choice of boundary conditions as well as to the choice of the parameters of the physical models is also performed. Finally the operation characteristics (such as the recirculation rate and the location of the reaction zone) of the furnace are evaluated.

1. Introduction

Flameless combustion [1], also known as Moderate and Intense Low-Oxygen Dilution (MILD) [2] or HiTAC combustion [3] is able to provide high combustion efficiency with low NO_x and soot emissions. The increasing interest in flameless combustion is motivated by the large fuel flexibility, representing a promising technology for low-calorific value fuels [4], high-calorific industrial wastes as well as in presence of hydrogen [5]. Moreover, flameless combustion is very stable and noiseless [6], so it could be potentially suited for gas turbine applications [7] where conventional operations may lead to significant thermo-acoustic instabilities ("humming") and stresses.

Flameless combustion needs the reactants to be preheated above their self-ignition temperature and enough inert combustion products to be entrained in the reaction region, in order to dilute the flame. As a result, the temperature field is more uniform than in traditional non-premixed combustion systems, and it does not show high temperature peaks. Hence, NO_x formation is suppressed as well as soot formation, due to the lean conditions, low temperatures and the large CO_2 concentration in the exhausts.

This combustion regime appears to be still worthy of further investigations and attention. In particular, the fundamental mechanism of the interaction between turbulent mixing and chemical kinetics needs to be elucidated. With respect to conventional flames, turbulence levels are enhanced (due to the high momentum of the gases), thus mixing timescales are reduced; on the contrary chemical timescales are increased due to dilution of the reactants [8]. In flameless combustion, the Damko□hler number approaches unity [9], implying that both mixing and chemical kinetics should be taken into account when modelling such a regime, resulting in a very challenging problem. In addition, most of the available models have been derived for conventional flames; hence they need to be validated and eventually revised for non-conventional regimes.

From a computational perspective, the role of the combustion model and the possible degree of simplification of chemical kinetics have not been rigorously and systematically assessed in the context of flameless combustion. Encouraging results in literature on the modelling of such flames have been found using the Eddy Dissipation Concept (EDC) model by Magnussen [10], coupled with detailed chemical mechanism. Such modelling strategy has been successfully applied to the Jet in Hot Coflow burner by Christo and Dally [11] and Aminian et al. [12]. The same approach leads to good results also in presence of hydrogen in the fuel, as reported by Parente et al. [13] and Galletti et al. [14]

for a self-recuperative burner and a lab-scale burner, respectively, operating in flameless combustion conditions.

However, recent investigations carried out by De et al. [15] and Aminian et al. [16] have indicated the need for revising the EDC constants in the framework flameless combustion modelling.

All the works reported above show that the oxidation scheme may strongly impact the results, as indicated by Shabanian et al. [17]. The global schemes are unsuited and generally lead to a strong over prediction of the flame temperatures. Recently Parente et al. [18] applied Principal Component Analysis to a set of measurements taken in flameless combustion conditions, showing that approaches based on single progress variable are not suited for the description of such combustion regime and finite-rate chemistry models are needed.

Finally, the modelling of NO emissions deserves also special attention. The Zeldovich thermal mechanism is the major contributor to NO in most of the conventional combustion system; however, in flameless combustion, the lower temperatures and the absence of large fluctuations inhibit NO formation through such a mechanism. As a result, NO emissions are controlled by other formation routes, such as the Fenimore's prompt NO and/or N_2O intermediate [19]. Therefore, it is necessary to incorporate all potentially relevant formation paths in the numerical model. Moreover, other routes may become relevant with non-conventional fuels, such as the NNH pathway for H_2 containing fuels [14]. The prediction of NO formation in flameless combustion, at low temperatures and with high concentration of H_2 in the fuel stream has been studied by Parente et al. [20]. They found that the inclusion of non-conventional NO formation routes, i.e. N_2O intermediate and NNH, is crucial for characterizing the pollutant emissions.

The elucidation of the above topics needs high fidelity and comprehensive experimental data to validate the numerical models. The Jet in Hot Coflow (JHC) burner [21], the Delft Jet in Hot Coflow (DJHC) [22-23] and the Cabra flame [24] have been conceived to emulate flameless conditions by feeding diluted and hot streams to the burner. They constitute a strong asset for the validation of numerical models as they have been equipped with advanced diagnostics to measure mean and fluctuating variables (e.g. chemical species, temperature, velocities).

However, in the industrial practice, flameless conditions are obtained by means of the massive internal recirculation of flue gases, which allows diluting the fresh gases before they reach the reaction zone. Such recirculation is generally achieved through special

designs of the feeding jets as well as of the combustion chamber. A recent review of different designs of flameless combustors is provided by Arghode and Gupta [25-26].

The recirculation affects both mixing and chemical timescales, so that conceptually these burners are different from JHC, DJHC and Cabra flames, which act solely on the chemical timescale. A few experimental investigations of flameless furnaces, based on internal recirculation of exhaust gases can be found in literature. Szegö et al. [19] described the performance and stability characteristics of a parallel jet flameless combustion burner system in a 20kW laboratory-scale furnace. Mi et al. [27] investigated a 20 kW recuperative MILD furnace, using EDC combustion model with global kinetic schemes for methane and ethane. Plessing et al. [28] and Ödzemir and Peters [29] provided a useful set of experimental data (velocity, temperature and NO emissions) on a 5.4 W furnace fed with methane and operating in flameless regime, subsequently modelled by Coelho and Peters [30] using the Eulerian Particle Flamelet model. Their results showed some discrepancies in the prediction of flow field as well as the overestimation of NO levels at the outlet section. Dally et al. [31] extended the investigation of the same furnace to more fuels and equivalence ratios. Verissimo et al. [32] experimentally investigated a 10 kW reversed-flow cylindrical furnace, for which simulation were performed by Graça et al. [33]. The Authors compared the EDC model coupled with the DRM-19 mechanism and the composition PDF (C-PDF) model, showing a general good agreement between predictions and experiments. Danon et al. [34] performed a parametric study on a 300 kW_{th} furnace equipped with three pairs of regenerative flameless combustion burners with the objective of optimizing the furnace performance. These experimental results were used as validation data for a set of Computational Fluid Dynamics (CFD) simulations of the furnace reported in [35]. The authors showed that the EDC model in combination with the realizable k-ε model and a skeletal chemistry mechanism allowed reproducing the main furnace performance for all the investigated burner configurations. Rebola et al. [36] performed an experimental investigation on a small-scale flameless combustor, defining the range of operating conditions allowing operating in flameless conditions. Cameretti et al. [37] discussed some aspects related to the employment of liquid and gaseous bio-fuels in a micro-gas turbine operating in flameless regime, showing numerically the energetic and environmental advantages related to the use of those fuels. Recently Huang et al. [38] studied the emissions from a flameless combustion staged combustor. The authors found

that the flameless regime yields lower NO emissions compared to the traditional diffusion combustion mode, and the N_2O intermediate mechanism dominates the NO production.

The present work aims at investigating the role of closure sub-models for the modelling of the flameless furnace of Plessing et al. [28] and Ödzemir and Peters [29], as well as at identifying the main NO formation paths. The selected experiment set-up was chosen as it represents an optimal compromise between lab-scale and industrial systems. It shows, in fact, the typical feature of industrial flames systems, i.e. the internal aerodynamic recirculation, allowing, at the same time, a sufficiently detailed characterization of the system performances.

While existing literature has pointed out the crucial role of finite rate chemistry models and detailed kinetics in flameless regime, little emphasis has been devoted to the quantification of the uncertainty related to the boundary conditions and physical models. The analysis focuses on the quantitative assessment of the scenario, i.e. boundary conditions, and modelling uncertainties on the results. In conjunction with appropriate validation metrics, this allows identifying the most sensitive parameters for the numerical simulations and developing a predictive model, which is accurate enough for the description of the system. Finally the operation characteristics (such as the recirculation rate and the location of the reaction zone) of the actual furnace are evaluated.

2. Test case

A sketch of the combustion chamber is provided for sake of clarity in Figure 1, even though all details of the system and experimental campaigns can be found in [28] and [29]. The combustion chamber is a parallelepiped (with 250x250 mm^2 cross-section and 485 mm length) with both the burner and the exhaust outlet placed at the bottom. The multi-nozzle burner consists of a central nozzle (inner diameter, i.d. = 4.7 mm) for fuel inlet; this nozzle is conically elevated 25 mm from the 6 peripheral nozzles (i.d. = 5 mm) for air inlet, located 40 mm away from the centre. The air nozzles are located 16 mm higher than the 15.5 mm wide annular exit (i.d. = 93 mm) for exhaust gases. The fuel is methane. Measurements were made for air and fuel mass flow rates of 6.5 and 0.38 kg/h, respectively, which correspond to an overall equivalence ratio $\varphi = 1$. Both fuel stream and air stream were preheated, to 650 K and 1150 K respectively.

3. Numerical simulations

The CFD model was defined using the commercial code Fluent 6.3 by Ansys Inc. The geometry and grid were realized using the software Gambit. Due to the combustion chamber symmetry, just a quarter of the geometry is considered for the numerical modelling. The grid, chosen after a mesh independency study, contained 501,000 cells; tetrahedrons were used near the burner zone, whereas hexahedral cells were used in the remainder of the furnace. The choice of a hybrid grid was aimed at reducing the number of cells required to discretize the computational domain accurately.

3.1 Boundary conditions

As far as boundary conditions are concerned, mass flow conditions were specified at both air inlets and fuel inlets; air inlet temperature is 1150 K whereas fuel inlet temperature is 650 K. A pressure outlet condition was employed for the exhaust gases exit. As far as walls are concerned, they were considered isothermal. The temperature of 1313 K was chosen, as suggested in [29]. For flameless condition operations, this appears an acceptable approximation, as supported in [1]. Simulations with fixed wall temperature were preferred over imposed heat flux boundary condition, since the latter exhibited numerical convergence problems, leading to unstable solutions and to the extinction of the combustion process. Simulations were also run considering a convective heat transfer at the wall, in order to verify the goodness of the isothermal hypothesis. The mean heat transfer coefficient, calculated from a global heat balance on the furnace, was evaluated at 7 W/m^2K, which is compatible with a natural convection process.

3.2 Physical models

Favre-averaged Navier-Stokes equations were solved, using the following turbulence models to resolve Reynolds stresses:

- Standard k–ε turbulence model (SKE) [39];
- Modified k–ε model (MKE) proposed by Morse [40] consisting in the variation of the first constant of the turbulent kinetic energy dissipation equation from 1.44 to 1.6;
- Renormalization group (RNG) k–ε [41];
- Realizable k–ε (RKE) [42];
- Reynolds Stress (RSM) model [43].

Radiation effects were accounted for using the Discrete Ordinate (DO) radiation model with the Weighted Sum of Gray Gases (WSGG) model for the participating media radiation, using the coefficients proposed by Smith et al. [44].

Turbulence-chemistry interactions were modelled using EDC [10]. As mentioned in the introduction, the EDC model is able to account for finite-rate effects and thus it can incorporate detailed kinetic schemes. Within the present study, four different kinetic schemes were used for methane oxidation:

- *JL scheme,* which is a 4-step global kinetic mechanism of Jones and Lindstedt [45], used both for methane and hydrogen-enriched fuels. It involves 7 species;
- *KEE58 scheme*, which is a skeletal mechanism made of 17 species and 58 chemical reversible reactions [46];
- *GRI 2.11 scheme,* which is a detailed mechanism. It was implemented without the NO_x reactions, resulting in 175 chemical reactions involving 31 species [47];
- *GRI 3.0 scheme*, which is a detailed mechanism. It was implemented without the NO_x reactions, resulting in 217 chemical reactions involving 35 species [48].

The In-Situ Adaptive Table (ISAT) [49] was coupled to EDC to reduce the computational costs. An error tolerance of 10^{-5} was selected to obtain table-independent results.

As for NO emissions, different formation routes were considered: thermal NO mechanism, Fenimore's Prompt mechanism and intermediate N_2O mechanisms. The thermal NO formation is modelled using a Finite Rate combustion model with a simplified one-step mechanism, obtained from the Zeldovich scheme by assuming a steady state for the N radicals and relating the O radical concentration to that of oxygen by means of the dissociation reaction [50]. The prompt NO formation is modelled following De Soete [51]. Finally, the N_2O intermediate mechanism is modelled according to the equation proposed by Malte et al [52].

All the above NO formation kinetic rates are integrated over a probability density function (PDF) for temperature, to account for the effect of temperature fluctuations on the mean reaction rates. The assumed PDF shape is that of a beta function [53] and is evaluated through the temperature variance, the latter solved by means of a transport equation.

3.3 Numerical settings

A second-order upwind discretization scheme was used for all equations and the SIMPLE algorithm was employed for pressure-velocity coupling. The simulations were run until the residuals for all the resolved quantities levelled out, resulting in a decrease of at least six

orders of magnitude. In addition flow field variables at different locations were monitored to check convergence to the steady state solution.

3.4 Validation metrics

In order to quantitatively measure the agreement between experimental data and computational predictions, validation metrics were employed, following Oberkampf and Barone [54].

For temperature, the average error metric normalized with respect to the measured value was evaluated, which is defined as:

$$\left|\frac{\bar{E}}{\bar{Y}_e}\right| = \frac{1}{N}\sum_{i=1}^{N}\left|\frac{Y_m - \bar{Y}_e}{\bar{Y}_e}\right| \quad (1)$$

where $\bar{Y}_e$ and Y_m are the mean measurement and the predicted value of variable Y.

For velocity measurements, it was chosen to refer to an absolute average error metric, defined as:

$$|\bar{E}| = \frac{1}{N}\sum_{i=1}^{N}|Y_m - \bar{Y}_e| \quad (2)$$

The choice of an absolute error metric for velocity measurements was justified by the need of avoiding division by zero in the error calculation. However, this kind of metric may not be enough to assess the goodness of the several models used. To better understand the deviation of predictions from measurements the Normalised Root-Mean-Square Error (*nrmse*) was also computed. This metric represents the sample standard deviation of the differences between the value predicted by a model and the value actually observed, divided by the range of observed values of the variable being predicted and it is defined as:

$$nrmse = \frac{\sqrt{\frac{\sum_{t=1}^{N}(Y_m - \bar{Y}_e)^2}{N}}}{\bar{Y}_{e,Max} - \bar{Y}_{e,Min}} \quad (3)$$

In addition, the quantitative agreement between predictions and experiments was also assessed with the coefficient of determination (R^2), from the parity plot of the axial velocity and the velocity fluctuations.

Beside the metrics provided by Equations 1-3, the construction of an error validation metric requires the estimation of the interval containing the true error. The latter is obtained from the evaluation of the intrinsic experimental error and the aleatory nature of the phenomenon under evaluation. The experimental data provided in [29] do not allow

quantifying these quantities in details, especially the statistical variability of the measurements, which requires a collection of multiple observations. Therefore, information from the literature [55] were used to estimate potential uncertainties in experimental observations, i.e. wall temperature, to evaluate the effect of uncertainties in boundary conditions on the results, as reported in Section 5.

4. Results

4.1 Effect of turbulence model

Figure 2 and Figure 3 show the comparison between experimental radial profiles of axial and radial velocity, respectively, and those predicted at different axial coordinates with different turbulence models and using the EDC model with KEE58 kinetic scheme.

The radial profile of axial velocity obtained very close to the burner exit (z = 0.012 m) shows an excellent agreement with experimental data with all turbulence models. At further distances the predicted data capture the trend, but typically predicted profiles are shifted towards larger distances. For the radial velocity, predicted values are generally lower that the measured ones for z = 0.012, 0.112 and 0.212 m, although the trend of the profile is captured.

Table 1 and Table 2 list the absolute average validation metrics as well as the *nrmse* for the profiles of axial and radial velocities as obtained with the different turbulence models. None of the turbulence models tested gives perfect agreement with experimental data. Moreover the behaviour of the different model is similar, with global absolute deviation from the measured value ranging from 2.84 to 4.06 m/s for the axial velocity (minimum value being 0.58 m/s with MKE and maximum value being 10.17 m/s with RNG) and from 0.92 to 0.99 m/s for the radial velocities (minimum value being 0.02 m/s with SKE and maximum value being 2.37 m/s with RNG). The same conclusions may be drawn considering the *nrmse*. The models that perform better are the SKE (0.31 for axial velocity and 0.59 for the radial one) and the RSM (0.29 for axial velocity and 0.61 for the radial one)

The comparison between experimental radial profiles of the axial component of velocity fluctuations and those predicted with different turbulence models is reported in Figure 4. Standard k-ε and RSM show the best agreement with the experimental data, even if some discrepancy can be noted. The absolute average validation metrics as well as the *nrmse* are shown in Table 3. Standard k-ε is indeed the model that provides the lowest deviation (0.5

m/s and 0.41 for *nrmse*), even though the other models show a quite similar behaviour (deviations ranging from 0.5 to 0.87 m/s, minimum value being 0.01m/s with SKE and maximum value being 4.41 m/s with MKE).

To confirm these observations, the coefficient of determination (R^2) for the parity plot of the measured and calculated velocities (Figure 5) are reported in Table 4. The standard k-ε model shows the best agreement with the experimental results (R^2 = 0.893 for axial mean velocity and R^2 = 0.869 for its fluctuation). As far as the radial velocity is concerned, the data show a low degree of correlation, also imputed to the small absolute values of velocity.

The prediction of the velocity field presented here is in line with the results provided by Coelho and Peters [30], who reported discrepancies between the measured and predicted velocity profiles. However, the lack of a discussion of the intrinsic uncertainties related to velocity measurements does not allow completely assessing the performances of the different turbulence models by means of the analysis of the predicted and measured velocity fields. Additional information is needed to select the turbulence model for the subsequent investigation of the effect of combustion models and kinetic mechanisms.

Figure 6a shows the measured temperature profiles along the combustion chamber axis and those obtained using the different turbulence models (with EDC and KEE58). The modified k-ε model provides the best results. Standard k-ε, RKE and RSM underestimate the temperature along the axis, while RNG yields higher temperature. The discrepancies in the temperature profile along the axis, provided by the different models are due to a completely different fluid dynamics of the flame. Relative error metrics were used in this case to quantitatively evaluate the agreement between experimental and predicted data. The modified k-ε model leads to an average deviation of about 2%, thus lower than the other models (6% for RNG, 7% for RKE and 8% for SKE and RSM). Based on these considerations, the MKE model was chosen for the following analysis.

4.2 Effect of the kinetic mechanism

As mentioned previously, since in flameless combustion regime the turbulence-chemistry interaction as well as the kinetic mechanism play a fundamental role, the EDC model coupled with four different kinetic schemes (JL, KEE58, GRI 2.11 and GRI 3.0) was considered. For all cases the turbulence model was the MKE.

The observation of axial and radial velocity profiles indicated that the kinetic scheme does not have a great influence the flow field predictions.

The predictions of the temperature field, however, are strongly affected by the choice of the kinetic scheme. This is well evident from Figure 6b, in which the measured temperatures along the axis of the chamber are compared with those predicted with the different kinetic schemes. The GRI 2.11 is the mechanism that performs better (average deviation 1.8 %), although also the KEE58 gives satisfactory results (average deviation 2%), confirming the necessity of taking into account at least skeletal kinetic mechanisms. The JL scheme over-predicts the temperature along the chamber axis (average deviation 7%), whereas the GRI 3.0 under-predicts it (average deviation 8%). Even though the GRI 3.0 is a detailed kinetic mechanism, it fails to predict flameless conditions, as also reported by Sabia et al [56].

4.3 Effect of wall boundary condition

The heat exchange at the wall has a major effect on the temperature profile inside the furnace. During the experimental campaign, the wall temperature at a distance z = 0.112 m was measured as 1313 K (1040 °C) [29]. Being flameless combustion characterized by a uniform temperature field, it was considered acceptable to carry out numerical simulations with walls at 1313 K. In order to verify the goodness of such hypothesis, also a convective heat transfer at the wall was considered. First a mean heat transfer coefficient was calculated, on the basis of a global heat balance on the furnace. The mean heat transfer coefficient is 7 W/m^2K, compatible with a natural convection process.

Figure 7 shows the temperature profile at different locations along the furnace wall using the heat transfer coefficient boundary condition. It can be observed that the temperature ranges from 1320K to 1380K, indicating that a temperature gradient exist and the temperature is not strictly constant at the wall. However, the relative temperature variation between the bottom and the top of the furnace is below 5%, thus indicating that the isothermal hypothesis for the wall is reasonable.

This is further confirmed by the analysis of Figure 8, which compares the predictions of the temperature along the axis of the furnace when the two different boundary conditions are considered. It is not possible to distinguish between the results obtained in the two cases, indicating that the type of boundary condition used at the wall does not significantly affect the predictions inside the furnace

4.4 NO emissions

As shown in the previous section, using different combustion/kinetic models leads to different temperature (and chemical species) distributions in the furnace. As a consequence NO emissions are predicted in a different way.

The experimental value for the NO emissions of the furnace (provided by Plessing et al [28]) is 10 ppm_v on dry basis. NO (on dry basis) predicted using different models are reported in Table 5**.** The GRI 2.11 and the KEE58 schemes perform similarly and yield to the best agreement with experimental NO data, predicted NO being respectively 8.1 and 8.7 ppm_v and experimental ones of 10 ppm_v. Conversely, the JL scheme provides NO emissions of 39.9 ppm_v, thus far from the experimental evidences, whereas the GRI 3.0 under-predicts the NO emissions by about 50 % (5.3 ppm_v).

Given the low temperatures, thermal NO formation does not play a major role. The contribution of the different pathways to the overall NO emissions is shown in Figure 9. It can be noticed the dominant role of the N_2O mechanism. In particular for the cases of GRI 2.11, KEE58 and GRI 3.0 models the N_2O mechanism is responsible for more than 80% of the NO production. With the JL scheme, however temperatures are higher so that the thermal mechanism dominates NO formation (99% of the NO production). This is due to the completely different prediction on the temperature field inside the furnace.

5. Uncertainty analysis

Validation cannot be carried out without explicitly accounting for the uncertainties present in both the measurements and the computation. As far as computation is regarded, the uncertainties are associated to the choice of the physical model and to the specification of the input parameters required for performing the analysis. The objective of the present section is to show how sensitive the numerical simulations are with respect to scenario parameters (boundary conditions) and model parameters. This appears crucial to identify the main sources of uncertainties and orient, therefore, modelling (and experimental) improvements.

The specification of the boundary conditions is a key issue in numerical simulation, and typically only limited information is available from corresponding experiments and observations. In the case of the furnace under investigation, the major uncertainty is related to the wall boundary condition. During the experimental campaign, the wall temperature at a distance z = 0.112 m was measured as 1313 K (1040 °C) [29]. Being flameless combustion characterized by a uniform temperature field, it was considered

acceptable to carry out numerical simulations with walls at 1313 K, as discussed in Section 3.1.

We can now assess the sensitivity of the numerical results to such a choice by modifying the wall temperature within a reasonable range of variability. Following the recent analysis provided by Parente et al. [55], who analysed the possible uncertainty sources for in-furnace temperature measurements, an uncertainty of ± 40K is considered here. Therefore, two temperature values were used to specify the furnace wall temperatures beside the base case discussed above: 1273 K and 1353 K. All the simulations were run using the modified k-ε turbulence model and the EDC combustion model coupled with the KEE58 chemical mechanism, since it allows having good results and saving computational time with respect to GRI 2.11.

Figure 10a shows the axial temperature profiles for these three cases. It is possible to notice that the wall temperature has a major effect on the temperature inside the chamber. In this case the best agreement with the experimental data is obtained when the value measured in the experimental campaign was considered.

In particular, when a lower temperature is considered, the maximum temperature inside the chamber decreases of 125 K with respect to the baseline case (T_w=1313 K), leading to an average deviation of 9%. On the other hand increasing the wall temperature leads to an average deviation of 7% and an increase of the maximum temperature of 80 K. Therefore, the propagation of the wall temperature uncertainty in the simulation results is slightly more than linear.

Following our discussion in Paragraph 4, the uncertainty related to the heat transfer coefficient, h, at the wall was also considered. A variation of 10% for h was considered therefore two additional simulations were run with h=6.3 W/m^{2}K and h=7.7 W/m^{2}K, respectively. Results are provided in figure 10b. When a lower coefficient is used, the temperature inside the furnace increases of 90K, while with the higher coefficient the temperature decreases of 60K, thus showing that the propagation of the uncertainty is slightly less than linear. This is an interesting result, showing that a convective heat transfer boundary conditions might be preferable over a fixed temperature one, since an error in the specification boundary condition would have a less significant effect on the results. The mean wall temperature is 1430 K with h=6.3 W/m^{2}K and 1304 K with h=7.7 W/m^{2}K.

It is also possible to compare the effect of the uncertainty in the boundary conditions to the one related to the choice of the physical models (i.e. turbulence, combustion and kinetic model).

Figure 10c and Figure 10d show the variability in the results related to the variation of the physical model and the kinetic mechanism, respectively. The uncertainties related to the boundary conditions and to the physical model are of the same order of magnitude. It is possible to notice a difference of 120 K on the maximum temperature inside the chamber as a result of the change in the physical model. The average deviation is 2% for MKE and 8% for SKE.

A larger uncertainty is associated with the choice of the kinetic mechanism. Switching from JL to GRI 3.0 leads to a difference on the maximum temperature of about 180 K. The relative average deviation is 1.8% for GRI 2.11, 2% for KEE58, 7% for JL and 8% for GRI 3.0. This confirms the importance of the choice of the kinetic mechanism and in the specific case of flameless furnaces, the necessity of taking into account detailed chemistry.

6. Operating characteristics of the furnace

Once the computational model is chosen and the uncertainties related to both models and boundary conditions are assessed, it is possible to evaluate some of the operating characteristics of the furnace, such as the recirculation rate k_R and the location of the reaction zone, in order to show that some of the theoretical characteristics of the flameless regime are actually present in the case under investigation.

In flameless combustion regime, the recirculation rate is a key parameter to quantify the amount of exhaust gases recirculated [1]. The recirculation rate is defined as the ratio between the net mass flow rate of recirculated flue gas and the sum of the fuel and air mass flow rates.

First a theoretic estimation of k_R is performed, following Cardoso [57], who relates recirculation rate, k_R, to the chamber-to-nozzle(s) areas by means of the parameter α:

$$k_R = 0.30\alpha^{1/1.59} \tag{3}$$

$$\alpha = \frac{1}{2}\left(\frac{A_c}{A_n} - 1\right) \tag{4}$$

where A_c is the section of the combustion chamber and A_n the section of the inlet nozzles. Using Equation 4, a value of 9.7 is obtained for k_R, in agreement with the value provided by provided by Plessing et al [28]

442 The value of k_R estimated using Equations 3 and 4 can be verified by post-processing the
443 CFD results. Starting from the flow streamlines inside the furnace, it is possible to locate
444 the plane on which the main recirculation takes place. The value of k_R is then calculated
445 from the following equation, reported in [1]:

$$k_R = \frac{\dot{m}_e}{\dot{m}_f + \dot{m}_a} \quad (5)$$

446 where $\dot{m}_e$ is the net mass flow rate of recirculated flue gas, whereas $\dot{m}_f$ and $\dot{m}_a$ are the
447 fuel and air mass flow rates, respectively. All those mass flow rates are calculating
448 following Equation 6:

$$\dot{m} = \int_S \rho v dS \quad (6)$$

449 The value provided by Equations 5 and 6 is k_R = 10.7, in excellent agreement with the
450 theoretical value calculated above.
451 In the conditions of the traditional combustion regime it is not possible to achieve
452 flammable mixtures of hydrocarbon and air for values of $k_R \geq 0.5$ without extinction
453 occurring, due to the lower oxygen concentration and higher inert species in the mixture.
454 However, the temperature and mixing ensured in the furnace allow the fuel to react in a
455 steady and stable form even for high values of the recirculation rate; this is the principle
456 behind flameless combustion [1-2].
457 As far as the reaction zone is concerned, it is possible to locate it considering the
458 distribution of two chemical species: the radical OH and the formaldehyde (CH_2O). Figure
459 11 shows the distribution of the mass fraction of OH and CH_2O across the furnace axis. It
460 is clear that the reaction zone is lifted, meaning that the reaction is taking place in diluted
461 condition and not as soon as the fuel and air jets mix.
462 In order to verify if the reaction is actually taking place in diluted condition the
463 distribution of the mass fraction of OH versus the mass fraction of O_2 is analysed. Figure
464 12 compares such distribution for three different flames:
465 - Flame C of the Sandia Laboratory [58], which is a purely diffusive flame;
466 - JHC burner [21], which emulates flameless conditions;
467 - Furnace under investigation.
468 As far as the first two systems are concerned, the experimental data were used, whereas for
469 the furnace under investigation the data obtained by the numerical model validated in the
470 previous sections are used.

It is possible to observe that for flame C (red stars) the reaction takes place for all the possible concentration of O_2, whereas for the JHC (blue crosses) the reaction takes place only in very diluted conditions. The furnace under investigation is a flameless system. However, a flameless-like behaviour can be only observed with an appropriate choice of combustion model and kinetic mechanism. To illustrate this, the mass fraction obtained with the KEE mechanism is plotted versus the mass fraction of O_2 (black circles). It can be observed that the combination EDC with KEE is able to predict that reactions mostly take place in diluted condition (mass fraction of O_2 below 0.06). A relatively small region where the reactions take place in presence of higher concentration of O_2 is also identified: the latter is probably associated to the ignition process, which is likely controlled by auto-ignition and takes place in diffusive conditions, as supported by recent investigations on the flameless combustion regime [59].

Therefore, we can conclude that the approach described in the previous sections lead to a comprehensive numerical model, which well describes the actual combustion system as indicated by the quantitative agreement between simulations and experimental observations. It should be stressed that the model development was not based on qualitative assessment and trial and error procedures, but it has been guided by a rigorous analysis of the possible sources of modelling and scenario uncertainties.

7. Concluding remarks

A numerical investigation through computational fluid dynamics of a semi-industrial furnace operating in flameless combustion mode has been presented. In particular the role of closure sub-models in flow field, temperature and NO emissions was studied.

Among the different turbulence models that were tested, the modified k-ε model provides the best agreement with the experimental data, especially as far as temperature is concerned. Reynolds stress model leads to a smaller deviation from the measured value when radial velocity and fluctuation velocity are concerned.

The Eddy Dissipation Concept (EDC), coupled with four different kinetic schemes (JL, KEE58, GRI 2.11 and GRI 3.0) was considered. The GRI 2.11 is the mechanism that performs better, although also the KEE58 gives satisfactory results, confirming the necessity of taking into account at least skeletal kinetic mechanisms.

As far as NO emissions are concerned, similar results were found. The GRI 2.11 and the KEE58 perform similarly and yield to the best agreement with experimental NO data.

The contribution of different formation routes was also examined. Given the low temperatures that characterize such combustion regime, the N_2O intermediate mechanism for formation of NO plays a major role, while thermal NO mechanism is not as relevant as in traditional combustion regime.

Finally an assessment of the uncertainty related to the choice of boundary conditions was performed. First, the effect of two different thermal boundary conditions was evaluated and then the uncertainty related to the value of the wall temperature and the value of the heat transfer coefficient was assessed. It was found that the wall temperature has a major effect on the temperature inside the chamber and this uncertainty is of the same order of magnitude as the uncertainty associated with the choice of the physical models. A larger uncertainty is associated to the kinetic mechanism, confirming that it plays a major role in the modelling of flameless furnaces.

Finally the operation characteristics of the furnace are evaluated. The recirculation rate k_R is estimated at 10.7 and it was found from the analysis of the radical OH distribution that the reaction takes place mostly in very diluted conditions.

The model obtained in the present work well agrees with the experimental data and it is the result of a rigorous analysis of the possible sources of modelling and scenario uncertainties.

References

1 Wünning J.A., Wünning J.G., Flameless oxidation to reduce thermal no-formation Prog. Energy Combust. Sci. 23 (1997) 81–94.

2 Cavaliere A., de Joannon M., Mild combustion, Prog. Energy Combust. Sci. 30 (2004) 329–66.

3 Gupta A.K., Thermal characteristics of gaseous fuel flames using high temperature air, J. Eng. Gas Turbines Power Transaction of ASME, 126 (2004), 9‑19.

4 Choi G.M., Katsuki M., Advanced low NO_x combustion using highly preheated air, Energy Convers. Manage. 42 (2001) 639–652.

5 Sabia P., de Joannon M., Fierro S., Tregrossi A., Cavaliere A., Hydrogen-enriched methane mild combustion in a well stirred reactor, Exp. Therm. Fluid Sci. 31 (2007) 469-475.

6 Duwig C., Stankovic D., Fuchs L., Li G., Gutmark, E., Experimental and numerical study of flameless combustion in a model gas turbine combustor, Combust. Sci. Technol. 180 (2008) 279-295.

537 7 Arghode V.K., Gupta A.K., Development of high intensity CDC combustor for gas turbine
538 engines, Applied Energy 88 (2011) 963-973.
539 8 Galletti C., Parente A., Tognotti L., Numerical and experimental investigation of a MILD
540 combustion burner, Combust. Flame 151 (2007) 649–664.
541 9 Isaac B.J., Parente A., Galletti C., Thornock J.N., Smith P.J., Tognotti L., A novel
542 methodology for chemical time scale evaluation with detailed chemical reaction kinetics,
543 Energy Fuels 27 (2013) 2255-2265.
544 10 Magnussen BF. On the structure of turbulence and a generalized eddy dissipation concept for
545 chemical reaction in turbulent flow. In: 19th AIAA aerospace science meeting, St. Louis,
546 Missouri; 1981.
547 11 Christo F.C., Dally B.B., Modeling turbulent reacting jets issuing in a hot coflow, Combust.
548 Flame 142 (2005) 117–129.
549 12 Aminian J., Galletti C., Shahhosseini S., Tognotti L., Key modeling issues in prediction of
550 minor species in diluted-preheated combustion conditions, Appl. Therm. Eng. 31 (2011)
551 3287-3300.
552 13 Parente A., Galletti C., Tognotti L., Effect of the combustion model and kinetic
553 mechanism on the MILD combustion in an industrial burner fed with hydrogen
554 enriched fuels, Int. J. Hydrogen Energy 33 (2008) 7553–7564.
555 14 Galletti C., Parente A., Derudi M., Rota R., Tognotti L., Numerical and experimental analysis
556 of NO emissions from a lab-scale burner fed with hydrogen-enriched fuels and operating in
557 MILD combustion, Int. J. Hydrogen Energy 34 (2009) 8339-8351.
558 15 De A., Oldenhof E., Sathiah P., Roekaerts D., Numerical simulation of Delft-jet-in-hot-coflow
559 (DJHC) flames using the Eddy Dissipation Concept model for turbulence-chemistry
560 interaction, Flow Turbul. Combust. 87 (2011) 537-567.
561 16 Aminian J., Galletti C., Shahhosseini S., Tognotti L., Numerical investigation of a MILD
562 combustion burner: analysis of mixing field, chemical kinetics and turbulence-chemistry
563 interaction, Flow Turbul. Combust. 88 (2012) 597-623.
564 17 Shabanian S.R., Medwell P.R., Rahimi M., Frassoldati A., Cuoci A., Kinetic and fluid
565 dynamic modeling of ethylene jet flames in diluted and heated oxidant stream combustion
566 conditions, Appl. Therm. Eng. 52 (2013) 538-554.
567 18 Parente A., Sutherland J.C., Dally B.B., Tognotti L., Smith P.J., Investigation of the MILD
568 combustion regime via Principal Component Analysis, Proc. Combust. Inst. 33 (2011), 3333-
569 3341.
570 19 Szegö G.G., Dally B.B., Nathan G.J., Scaling of NO_x emissions from a laboratory scale MILD
571 combustion furnace, Combust. Flame 154 (2008) 281-295.
572 20 Parente A., Galletti C., Tognotti L., A simplified approach for predicting NO formation in

MILD combustion of CH_4-H_2 mixtures, Proc. Combust. Inst. 33 (2011) 3343-3350.

21 Dally B.B, Karpetis, Barlow R., Structure of turbulent nonpremixed jet flames in a diluted hot coflow, Proc. Comb. Inst. 29 (2002) 1147–1154.

22 Oldenhof E., Tummers M.J., Van Veen M.H., Roekaerts D.J.E.M., Ignition kernel formation and lift-off behavior of jet in hot coflow flames, Combust. Flame 157 (2010) 1167-1178.

23 Oldenhof E., Tummers M.J., Van Veen M.H., Roekaerts D.J.E.M., Role of the entrainment in the stabilization of jet in hot coflow flames, Combust. Flame 158 (2011) 1553-1563.

24 Cabra, R., Chen, J.Y., Dibble, R.W., Karpetis, A.N. and Barlow R.S., Lifted methane-air jet flames in a vitiated coflow, Combust. Flame 143 (2005) 491–506.

25 Arghode V.K., Gupta A.K., Investigation of forward flow distributed combustion for gas turbine application, Applied Energy 88 (2011) 29-40.

26 Arghode V.K., Gupta A.K., Investigation of reverse flow distributed combustion for gas turbine application, Applied Energy 88 (2011) 1096-1104.

27 Mi J., Li P., Zheng C., Numerical simulation of flameless premixed combustion with an annular nozzle in a recuperative furnace, Chin. J. Chem. Eng., 18 (2010) 10-17.

28 Plessing, T. Peters, N. and Wünning, J.G Laser optical Investigation of Highly Preheated Combustion with Strong Exhaust Gas Recirculation *Twenty-Seventh Symposium (Int.) on Combustion,* The Combustion Institute, Pittsburgh, PA, (1998), 3197–3204.

29 Özdemir B.I., Peters N., Characteristics of the reaction zone in a combustor operating at mild combustion, Exp. Fluids 30 (2001) 683– 695.

30 Coelho P.J., Peters N., Numerical simulation of a MILD combustion burner Combust. Flame 124 (2001) 503–518.

31 Dally B.B., Riesmeier E., Peters N., Effect of fuel mixture on moderate and intense low oxygen dilution combustion, Combust. Flame 137, (2004), 418-431.

32 Verissimo A.S., Rocha A.M.A., Costa M., Importance of the inlet air velocity on the establishment of flameless combustion in a laboratory combustor, Exp. Therm. Fluid Sci. 44 (2013) 75-81.

33 Graça M., Duarte A., Coelho P.J., Costa M., Numerical simulation of a reversed flow small-scale combustor, Fuel Proces. Techn. 107 (2013) 126-137.

34 Danon B., Cho E.S., de Jong W., Roekaerts D.J.E.M., Parametric optimization study of a multi-burner flameless combustion furnace, Appl. Therm. Eng. 31 (2011) 3000-3008.

35 Danon B., Cho E.S., de Jong W., Roekaerts D.J.E.M., Numerical investigation of burner positioning effects in a multi-burner flameless combustion furnace, Appl. Therm. Eng. 31 (2011) 3885-3896.

607 36 Rebola A., Costa M., Coelho P.J., Experimental evaluation of the performance of a flameless
608 combustor, Appl. Therm. Eng. 50 (2013) 805-815.
609 37 Cameretti M.C., Tuccillo R., Piazzesi R., Study of an exhaust gas recirculation equipped
610 micro gas turbine supplied with bio-fuels, Appl. Therm. Eng. 59 (2013) 162-173.
611 38 Huang M., Shao W., Xiong Y., Liu Y., Zhang Z., Lei F., Xiao Y., Effect of fuel injection
612 velocity on MILD combustion of syngas in axially-staged combustor, Appl. Therm. Eng. 66
613 (2014) 485-492.
614 39 Launder B.E., Spalding D.B., The numerical computation of turbulent flows, Comp. Meth.
615 Appl. Mech. Eng. 3 (1974) 269-289.
616 40 Morse A.P., Axisymmetric turbulent shear flows with and without swirl, Ph.D. Thesis.
617 England: London University, 1977.
618 41 Yakhot V., Orszag S.A., Renormalization group and local order in strong turbulence, Nuclear
619 Physics B 2 (1987) 417-440.
620 42 Shih T.H., Zhu J., Lumley J., A realizable algebraic stress model, Symp. on Turbulent Shear
621 Flow, Kyoto (Japan), Paper 3.5, (1993).
622 43 Launder B.E., Reece G.J., Rodi W., Progress in the development of a Reynolds-Stress
623 turbulence closure, J. Fluid Mech. 68 (1975) 537-566.
624 44 Smith T.F., Shen Z.F., Friedman J.N., Evaluation of Coefficients for the Weighted Sum of
625 Gray Gases Model, J. Heat Transfer 104 (1982) 602-608.
626 45 Jones W.P., Lindstedt R.P., Global reaction schemes for hydrocarbon combustion, Combust.
627 Flame 73 (1988) 233-249.
628 46 Bilger R.W., Starner S.H., Kee R.J., On Reduced Mechanisms for. Methane-Air Combustion
629 in Nonpremixed Flames, Combust. Flame 80 (1990) 135-149.
630 47 Bowman C.T., Hanson R.K., Davidson D.F., Gardiner W.C., Lissianski V., Smith G.P.,
631 Golden D.M., Frenklach M., Goldenberg M., www.me.berkeley.edu/gri_mech/ (last accessed
632 09/09/2014).
633 48 Smith P.G., Golden D.M., Frenklach M., Moriarty N.W., Eiteneer B., Goldenberg M.,
634 Bowman C.T., Hanson R.K., Song S., Gadiner W.C. Jr., Lissianski V.V., Qin Z.,
635 www.me.berkeley.edu/gri_mech/ (last accessed 09/09/2014).
636 49 Pope S.B., Computationally efficient implementation of combustion chemistry using *in situ*
637 adaptive tabulation, Combust. Theory Modeling 1 (1997) 41-63.
638 50 Westenberg A.A, Kinetics of NO and CO in Lean, Premixed hydrocarbon-air flames,
639 Combust. Sci. Tech. 4 (1971) 59-64.
640 51 De Soete G.G.D., Overall reaction rates of NO and N_2 formation from fuel nitrogen, Proc.
641 Comb. Inst. 15 (1974) 1093-1102.

642 52 Malte P.C., Pratt D.T., Measurement of atomic oxygen and nitrogen oxides in jet stirred
643 combustion, Proc. Comb. Inst. 15 (1974) 1061–1070.
644 53 Peters N., Turbulent Combustion, Cambridge University Press, UK, 2001.
645 54 Oberkampf W.L., Barone M.F., Measures of agreement between computation and experiment:
646 validation metrics, J. Comput. Phys. 217 (2006) 5-36
647 55 Parente A., Coraggio G., Galletti C., Tognotti L., Verification, validation and uncertainty
648 quantification: some practical tools, IFRF report G 25/y/01, Livorno, 2011.
649 56 Sabia P., de Joannon M., Picarelli A., Chinnici A., Ragucci R., Modeling negative
650 temperature coefficient region in methane oxidation, Fuel 91 (2012) 238-245.
651 57 Cardoso D., Relations between global recirculation rate and area ration in combustors fired
652 with jets, Heat Processing 9 (2011) 253-255.
653 58 Barlow R.S., Frank J.H., Relations between global recirculation rate and area ration in
654 combustors fired with jets, Proc. Combust. Inst. 27 (1998) 1087-1095.
655 59 Stankovic I., Merci B., Analysis of auto-ignition of heated hydrogen air mixtures with
656 different detailed reaction mechanisms, Combust. Theory Model. 15 (2011) 409-436.

Table 1 - Average absolute validation metrics [m/s] and Normalised Root-Mean-Squared Error [-] for axial velocity with different turbulence models. EDC, KEE58.

z [m]	Average Absolute Metrics [m/s]					Normalised Root-Mean-Squared Error [-]				
	MKE	SKE	RNG	RKE	RSM	MKE	SKE	RNG	RKE	RSM
0.012	2.77	2.25	2.99	2.82	2.18	0.09	0.08	0.10	0.09	0.08
0.112	4.56	4.64	5.90	4.27	4.20	0.45	0.40	0.51	0.39	0.37
0.212	3.95	3.23	3.25	4.67	2.82	0.40	0.30	0.40	0.36	0.27
0.312	5.00	2.79	3.19	4.41	2.60	0.87	0.47	0.53	0.77	0.44
Total	4.06	2.84	3.42	3.95	2.95	0.45	0.31	0.38	0.40	0.29

Table 2 - Average absolute validation metrics [m/s] and Normalised Root-Mean-Squared Error [-] for radial velocity with different turbulence models. EDC, KEE58

z [m]	Average Absolute Metrics [m/s]					Normalised Root-Mean-Squared Error [%]				
	MKE	SKE	RNG	RKE	RSM	MKE	SKE	RNG	RKE	RSM
0.012	1.31	1.48	1.16	1.38	1.08	0.67	0.78	0.59	0.70	0.55
0.112	0.39	0.23	0.31	0.31	0.23	0.71	0.42	0.57	0.56	0.47
0.212	0.53	0.50	0.51	0.49	0.60	0.69	0.68	0.68	0.64	0.81
0.312	0.17	0.15	0.16	0.15	0.18	0.58	0.48	0.52	0.53	0.62
Total	0.99	0.98	0.92	0.98	0.92	0.66	0.59	0.59	0.61	0.61

Table 3 - Average absolute validation metrics [m/s] and Normalised Root-Mean-Squared Error [-] for axial component of velocity fluctuations with different turbulence models. EDC, KEE58.

z [m]	Average Absolute Metrics [m/s]					Normalised Root-Mean-Squared Error [%]				
	MKE	SKE	RNG	RKE	RSM	MKE	SKE	RNG	RKE	RSM
0.012	1.40	0.90	1.35	1.32	1.38	0.25	0.15	0.22	0.22	0.23
0.112	0.46	0.55	0.73	0.63	0.55	0.25	0.30	0.42	0.34	0.29
0.212	0.90	0.54	0.33	1.03	0.62	0.67	0.45	0.25	0.80	0.51
0.312	0.77	0.40	0.15	0.82	0.42	1.32	0.72	0.36	1.49	0.73
Total	0.77	0.50	0.62	0.80	0.61	0.62	0.41	0.31	0.71	0.44

Table 4 - Coefficient of determination (R^2) for axial velocity and axial component of velocity fluctuations with different turbulence models. EDC, KEE58.

	MKE	SKE	RNG	RKE	RSM
Axial velocity	0.826	0.893	0.880	0.846	0.876
Velocity fluctuations (RMS)	0.787	0.869	0.645	0.752	0.775

Table 5 - Comparison between experimental NO emissions [ppm_v] and those predicted using different kinetic schemes.

Exp.	JL	KEE58	GRI2.11	GRI3.0
10	39.9	8.7	8.1	5.3

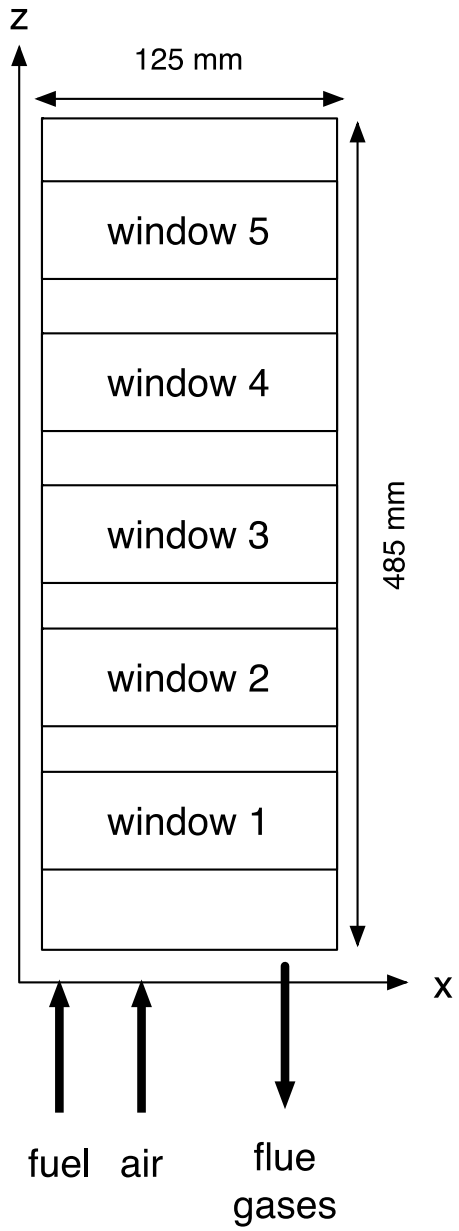

Figure 1 - Sketch of the experimental furnace [30].

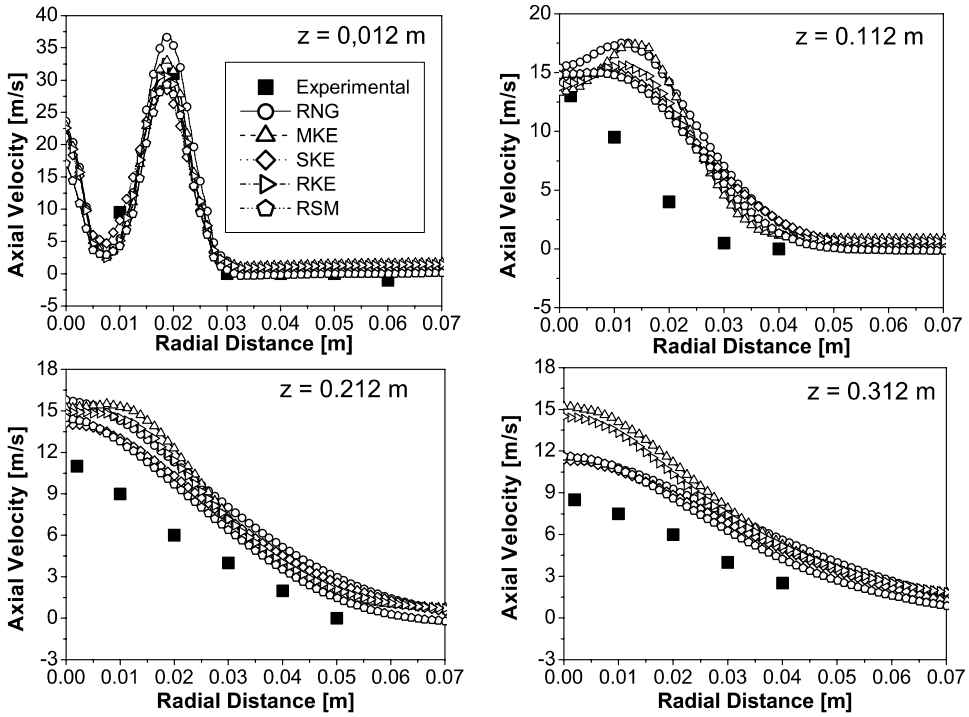

Figure 2 - Comparison between experimental axial velocity profiles and those predicted with different turbulence models, at different axial coordinates. EDC combustion model, KEE58 kinetic mechanism.

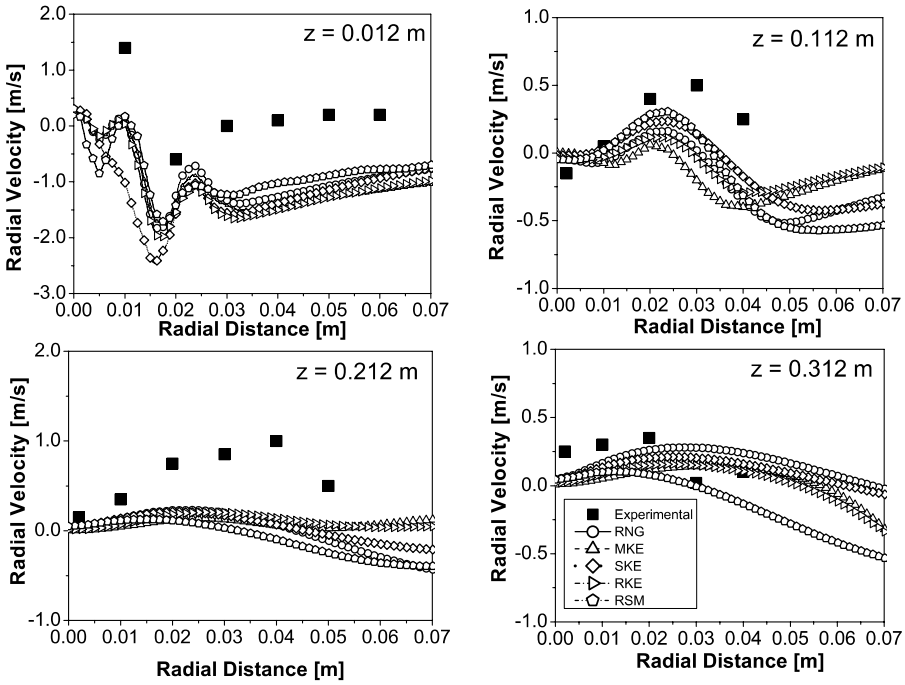

Figure 3 - Comparison between experimental radial velocity profiles and those predicted with different turbulence models, at different axial coordinates. EDC combustion model, KEE-58 kinetic mechanism.

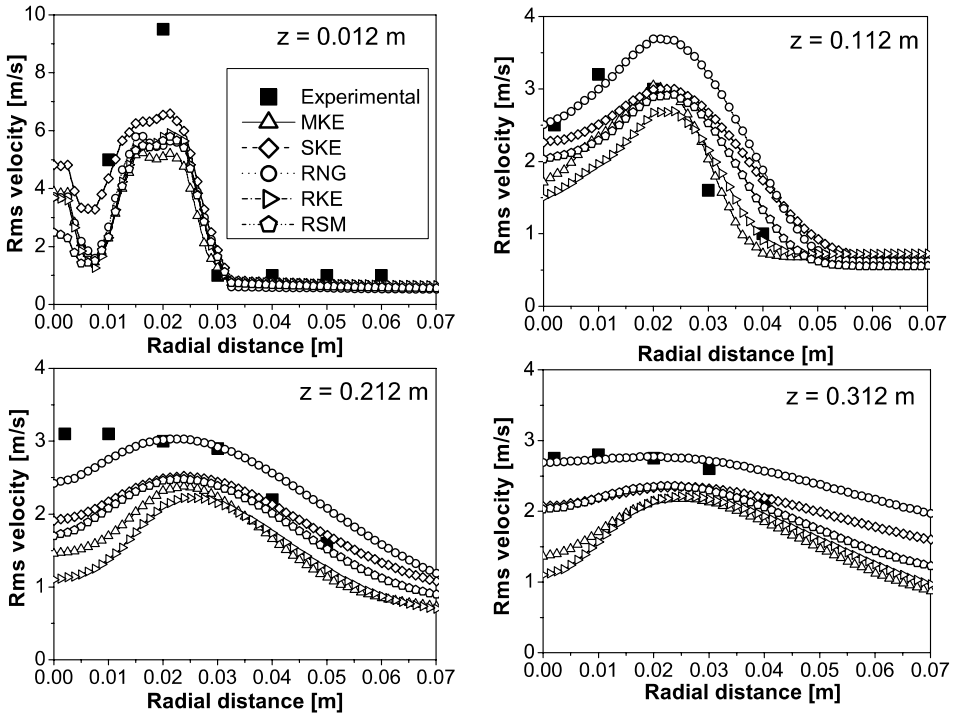

Figure 4 - Comparison between experimental radial profiles of the axial component of velocity fluctuations and those predicted with different turbulence models, at different axial coordinates. EDC combustion model, KEE58 kinetic mechanism.

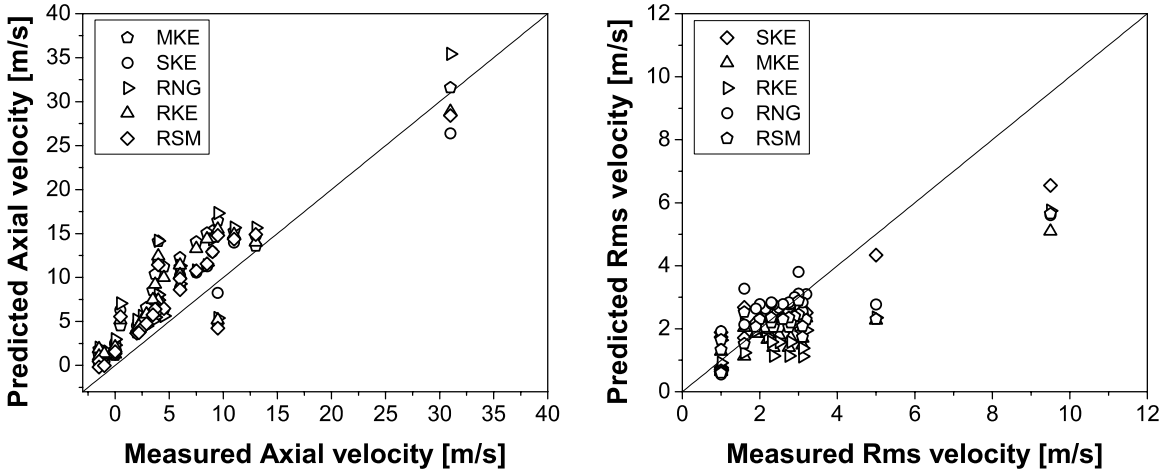

(a) (b)

Figure 5 – Parity plot of measured and predicted values of axial (a) mean velocity and (b) velocity fluctuation, for different turbulence models. EDC combustion model, KEE58 kinetic mechanism.

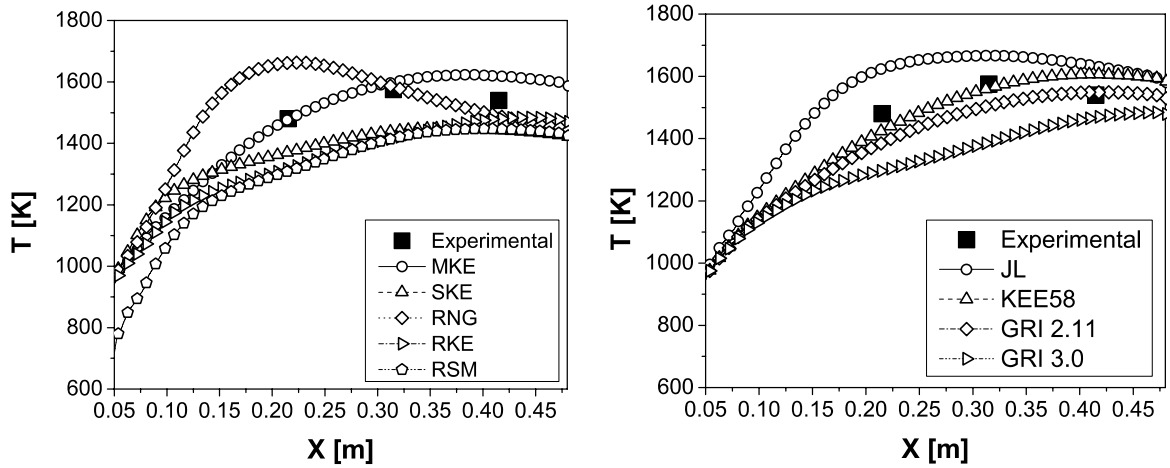

(a) (b)

Figure 6 - Comparison between experimental temperature profile along the combustion chamber axis and those predicted with (a) different turbulence models and (b) different kinetic mechanisms. MKE turbulence model, EDC combustion model.

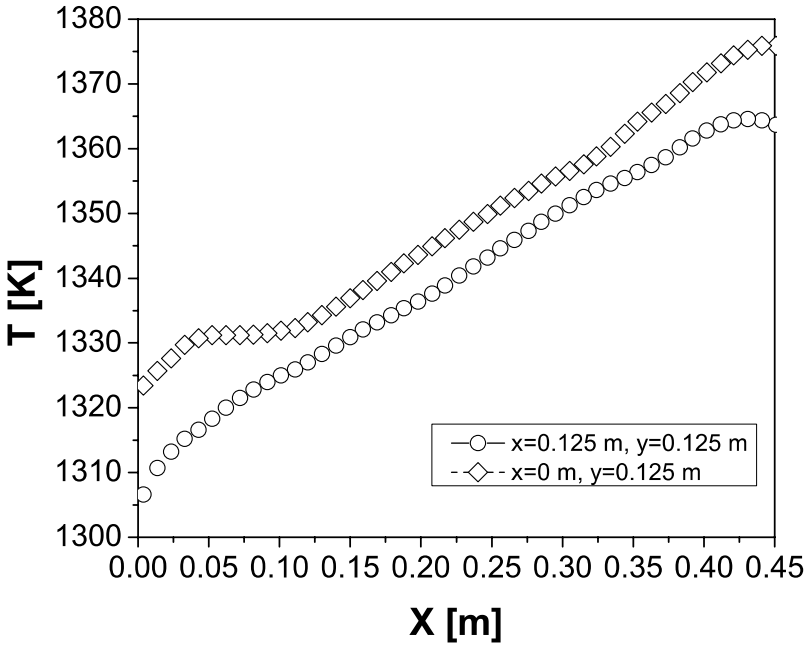

Figure 7 – Temperature profiles at different locations along the furnace wall, predicted with a convective heat transfer wall boundary condition. MKE turbulence model, EDC combustion model, KEE58 kinetic mechanism.

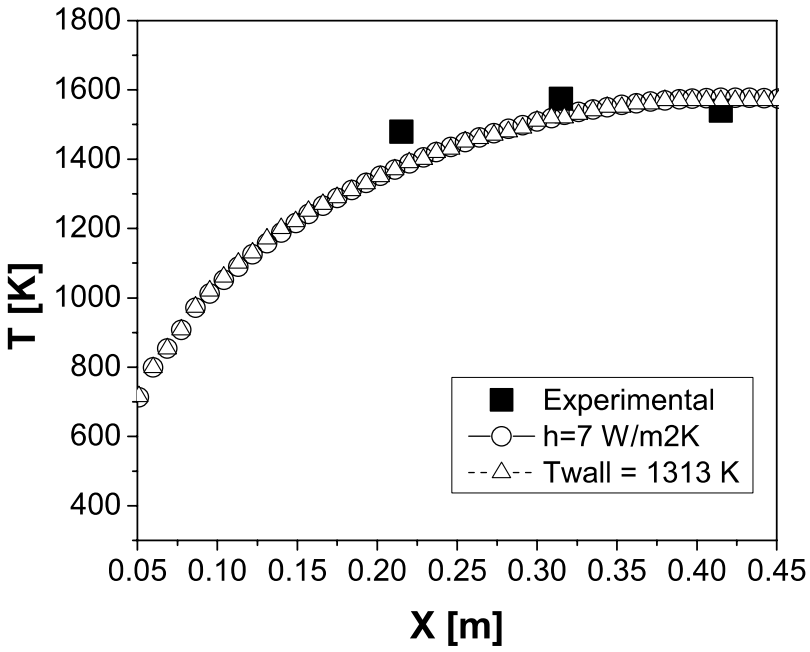

Figure 8 - Comparison between experimental temperature profile along the combustion chamber axis and those predicted with different wall boundary conditions. MKE turbulence model, EDC combustion model, KEE58 kinetic mechanism.

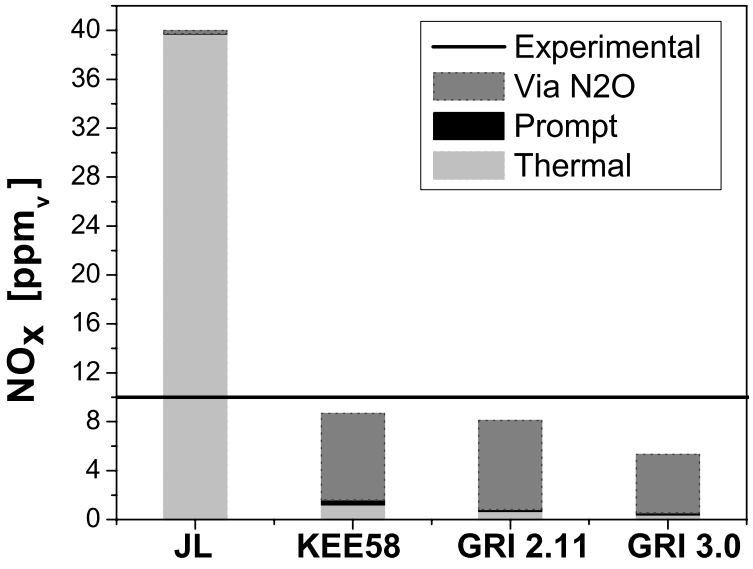

Figure 9 - Contribution of different formation routes to the total NO emissions (dry basis), predicted with different kinetic mechanisms. MKE turbulence model, EDC combustion model.

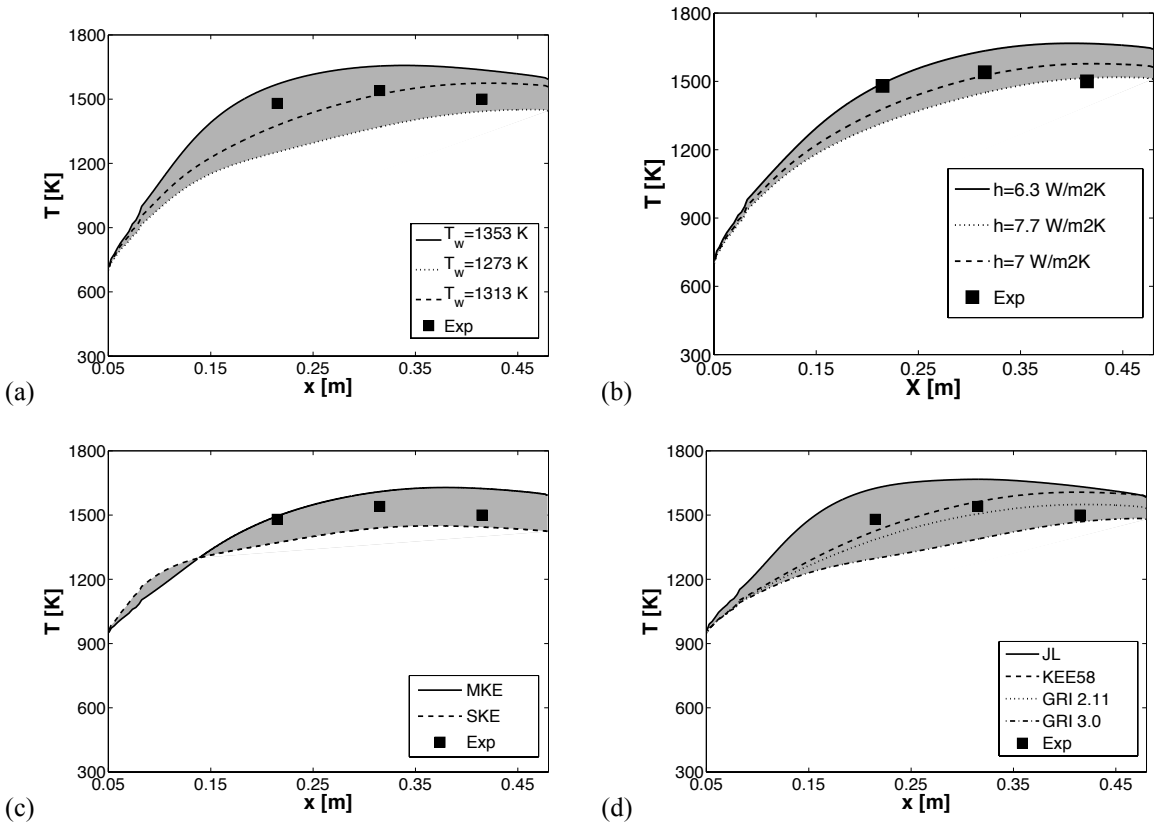

Figure 10 - Uncertainty on axial temperature predictions, associated with (a) the wall temperature boundary conditions, (b) the heat transfer coefficient, (c) the turbulence model and (d) the kinetic mechanism. EDC combustion model, KEE58 kinetic mechanism.

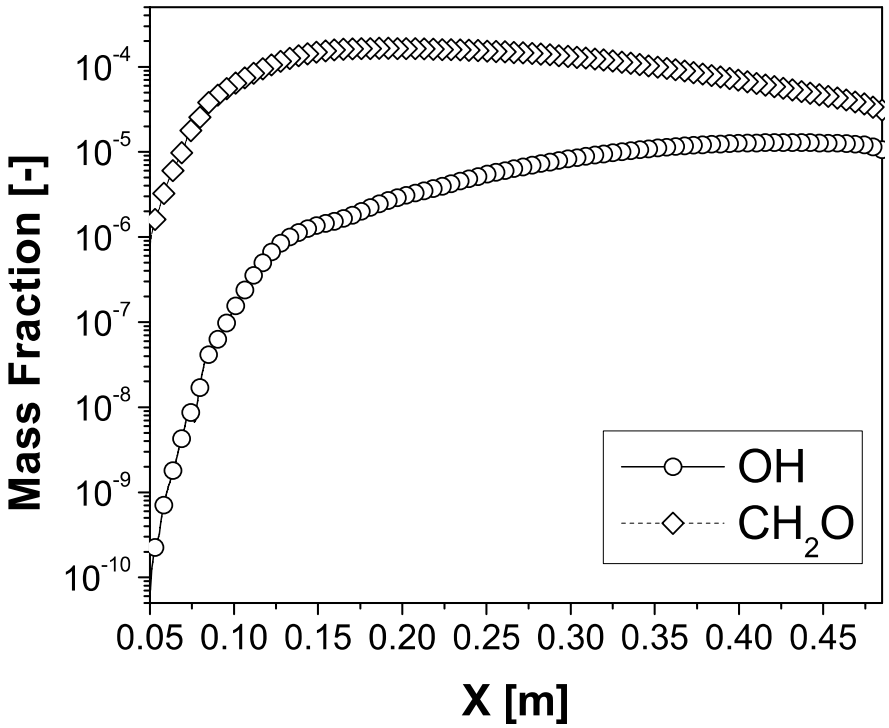

Figure 11 - OH and CH_2O mass fraction distribution along the furnace. MKE turbulence model, EDC combustion model, KEE58 kinetic mechanism.

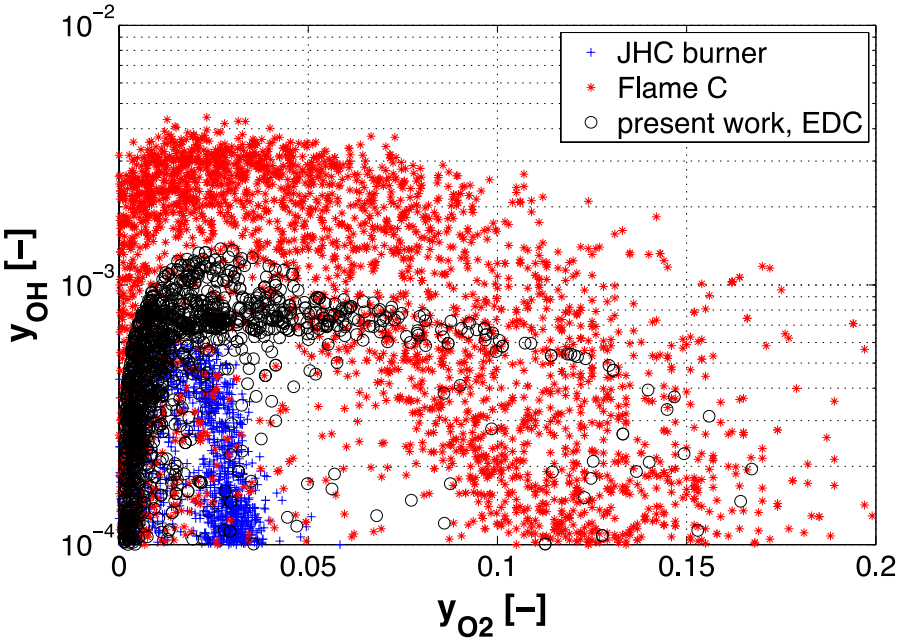

Figure 12 - Distribution of the mass fraction of OH versus the mass fraction of O_2 for Flame C, JHC and the furnace under investigation.